AIAA 2003–3111

Aeroacoustic Analysis of a Simplified Landing Gear

David P. Lockard and Mehdi R. Khorrami
NASA Langley Research Center
Hampton, VA 23681

Fei Li
High Technology Corporation
Hampton, VA

10th AIAA/CEAS Aeroacoustics Conference
May 12–14, 2003
Hilton Head, SC

AEROACOUSTIC ANALYSIS
OF A SIMPLIFIED LANDING GEAR

David P. Lockard,* Mehdi R. Khorrami†

NASA Langley Research Center

Hampton, VA

and

Fei Li

High Technology Corporation

Hampton, VA

This paper investigates the noise generated by a simplified landing gear without small scale parts such as hydraulic lines and fasteners. The Ffowcs Williams and Hawkings equation is used to predict the noise at far-field observer locations from surface pressure data provided by an unsteady computational fluid dynamics calculation. Beyond prediction, the analysis involves identifying the parts of the landing gear responsible for different features in the spectra. Because of the simplified nature of the model, most of the unsteadiness is restricted to low frequencies. The gear boxes and oleo appear to be the primary sources of unsteadiness at these frequencies. Interpretation of the data is complicated by discretization errors at grid blocks with patched boundaries in the computational fluid dynamics calculation which appear to be dominant on the flat plate above the gear. Nonetheless, the calculations demonstrate the utility of large scale computations for improving the understanding of landing gear noise.

Nomenclature

c	speed of sound
f	integration surface defined by $f = 0$
F_i	dipole source terms
H	Heaviside function
i	$\sqrt{-1}$
M_i	local source Mach number vector, v_i/c
M	Mach number, $|M_i|$
$\hat{n}_i$	outward directed unit normal vector
p	pressure
$\mathbf{Q}$	monopole source term
t	time
u_i	Cartesian fluid velocity components
v_i	Cartesian surface velocity components
x, y, z	Cartesian observer coordinates

Greek:

$\delta(f)$	Dirac delta function
δ_{ij}	Kronecker delta
ρ	fluid density
ξ, η, ζ	source coordinates

Superscript:

$'$	perturbation quantity (e.g. $\rho' = \rho - \rho_o$)

Subscript:

o	freestream quantity

Introduction

The past thirty years have seen significant reductions in jet noise through the adoption of high-bypass-ratio turbofan engines on civil aviation transports. Formerly unimportant noise sources such as the airframe have now become a major concern for noise certification and environmental considerations. Airframe noise is most important during aircraft approach and landing, when engines are operating at reduced thrust with the high-lift devices and landing gear deployed. Wind tunnel tests and fly-over measurements have revealed the leading-edge slats, flap edges, and the landing gear to be the major contributors to airframe noise. Each of the three primary sources of airframe noise are important on different classes of airplanes, but the main landing gear is a dominant source on most modern widebody transports. Although flow computations of high-lift devices such as flaps and slats received considerable attention in the last decade, the intricacies of a landing gear flow field and its associated sound sources have remained virtually unknown due to overwhelming geometrical complexities. In this paper, we present a preliminary analysis of our computational aeroacoustic study of a model landing gear. Our computational approach involves a hybrid strategy. In the first step we perform an unsteady Reynolds Averaged Navier-Stokes (URANS) simulation to provide a highly resolved near-field solution. Despite continued advances in computational resources and numerical algorithms, it is still prohibitively expensive and often infeasible to attempt to resolve wave propagation from near-field

sources to far-field observers. Integral techniques that can predict the far-field signal based solely on near-field input are a means to overcome this difficulty. Hence, the Ffowcs Williams-Hawkings (FW-H) equation[1] solver described by Lockard[2] is used to predict the acoustic signature at various observer locations using surface pressure data from the computational fluid dynamics (CFD) calculation.

Acoustic Equations

The FW-H equation can be written in differential form[3] as

$$\left(\frac{\partial^2}{\partial t^2} - c_o^2 \frac{\partial^2}{\partial x_i \partial x_i}\right)\left(H(f)\rho'\right) =$$
$$\frac{\partial^2}{\partial x_i \partial x_j}\left(T_{ij}H(f)\right)$$
$$- \frac{\partial}{\partial x_i}\left(F_i\delta(f)\right) + \frac{\partial}{\partial t}\left(Q\delta(f)\right) \quad (1)$$

where

$$T_{ij} = \rho u_i u_j + P_{ij} - c_o^2\rho'\delta_{ij}, \quad (2)$$

$$F_i = \left(P_{ij} + \rho u_i(u_j - v_j)\right)\frac{\partial f}{\partial x_j}, \text{ and} \quad (3)$$

$$Q = \left(\rho_o v_i + \rho(u_i - v_i)\right)\frac{\partial f}{\partial x_i}. \quad (4)$$

The dipole term F_i involves an unsteady force, and Q gives rise to a monopole-type contribution that can be thought of as an unsteady mass addition. The function $f = 0$ defines the surface outside of which the solution is desired. The normalization $|\nabla f| = 1$ is used for f. The total density and pressure are given by ρ and p, respectively. The fluid velocities are u_i, while the v_i represent the velocities of the surface f. The Kronecker delta, δ_{ij}, is unity for $i = j$ and zero otherwise. The ambient speed of sound is denoted by c_o. A prime is used to denote a perturbation quantity relative to the free-stream conditions denoted by the subscript o. The Cartesian coordinates and time are x_i and t, respectively. The usual convention, which is followed here, involves a quiescent ambient state with f prescribed as a function of time so that it always surrounds a moving source region of interest. $H(f)$ is the Heaviside function which is unity for $f > 0$ and zero for $f < 0$. The derivative of the Heaviside function $H'(f) = \delta(f)$ is the Dirac delta function, which is zero for $f \neq 0$, but yields a finite value when integrated over a region including $f = 0$. The inviscid part, $P_{ij} = p\delta_{ij}$, of the compressive stress tensor P_{ij} is used in this work.

The FW-H equation is an exact rearrangement of the Navier-Stokes equations that allows one to determine the acoustic signal at distant observer locations if the details of the source region are already known. Hence, the Navier-Stokes equations still need to be solved, but only where

nonlinear and viscous effects are important. All of the linear propagation can be determined by the FW-H equation. For three-dimensional flows, the time-domain FW-H formulations developed by Farassat[4] are efficient and amenable to numerical computations. Some additional efficiency can be obtained by restricting the source to uniform, rectilinear motion. Furthermore, the equation can be solved in the frequency domain which can be useful if one is only interested in analyzing certain frequencies. The frequency domain solution of FW-H equation can be written in the form[2]

$$H(f)c_o^2\rho'(\mathbf{y},\omega) = -\int_{f=0} F_i(\boldsymbol{\xi},\omega)\frac{\partial G(\mathbf{y};\boldsymbol{\xi})}{\partial y_i}\,ds$$
$$- \int_{f=0} i\omega Q_n(\boldsymbol{\xi},\omega)G(\mathbf{y};\boldsymbol{\xi})\,ds + I_Q \quad (5)$$

where

$$F_i = \left(p\delta_{ij} + \rho(u_i - U_i)(u_j + U_j) + \rho_o U_i U_j\right)\hat{n}_j,$$

$$Q_n = \left(\rho(u_i + U_i) - \rho_o U_i\right)\hat{n}_i. \quad (6)$$

The quadrupole term is denoted by I_Q and includes effects such as nonlinear propagation and refraction. In this work, the quadrupole contribution is expected to be small and is neglected. Souliez et al.[5] performed FW-H predictions of landing gear noise using solid and porous integration surfaces and found the solutions to be nearly identical in the far-field, although discrepancies were noted in the near field. The porous surface enclosed a significant region around the gear and should have included most of the quadrupole effects. In this work, our attention is restricted to the far-field where it should be valid to neglect the quadrupole.

Source Identification

By examining equation 5, it is apparent that the contribution to the noise from each portion of the integration surface combines linearly to form the signal. Hence, one can calculate the noise from different sections of the integration surface and see how the resulting noise compares to the total. Although this is a useful diagnostic, interpretation can be difficult when acoustic shielding occurs. For example, if an observer is in a shadow region, the contributions from different subsurfaces can be nonnegligible, but the summed result is zero. Examination of how the solution varies with observer location combined with information about the geometry usually makes it apparent whether such a phenomena is occurring.

Another method for identifying source locations involves querying the function that is being integrated. For

a given frequency of interest, the integrand in equation 5 can be plotted over the entire integration surface to visually show where the noise is being generated. For the impenetrable surface data being used in this investigation, the integrand is extremely simple. On solid surfaces, $u_j = -U_j$ and equations 6 simplify to

$$Q = -\rho_o U_i \hat{n}_i \ \text{ and } \ F_i = (p + \rho_o U_i U_j)\hat{n}_i. \quad (7)$$

Note that Q and $\rho_o U_i U_j$ are steady in time and therefore have no impact on the frequency domain solution. Hence, only the pressure is needed. The amplitude of the complex integrand for each frequency can be plotted over the surface of the gear to give an indication of potential noise sources. Again, one can be deceived by the results because the phase information is lost when the amplitude of the complex integrand is plotted. By examining the real and imaginary components, one can get an idea of whether the signals will combine constructively or destructively. Additional corroboration should be sought by examining the underlying CFD calculation to determine if there are any flow features present that could account for the unsteadiness generating the noise. Interpreting the results in conjunction with the geometry of the model and the physics of the flow being examined usually presents a clear picture of the noise sources.

Although these source identification techniques can incorrectly indicate where the noise is being generated, all true noise sources are usually identified. Because the ultimate goal is to identify the flow features giving rise to the noise, one has to query the CFD solution in the volume surrounding the potential source regions simultaneously. It usually becomes apparent whether any fluid structure could possibly be generating noise at the locations identified by the analysis. The advantage of doing the analysis is that it significantly reduces the number of locations where one needs to look.

Simplified Landing Gear Model

The simulated geometry is a four-wheel landing gear model that approximately represents a ten percent scale Boeing 757 main landing gear. The model geometry is fairly complex and composed of four wheels, two side struts, an oleo, a side-door, yokes, a pin, and other structures that join the system together (Figure 1 (a)). The gear assembly is mounted on a flat plate that represents the aircraft wing. The structured grid consists of 155 blocks possessing a total of 1.8 million grid points. Figure 1(a) also shows the grid distribution on the surface of the landing gear. The reference length scale is the gear wheel diameter (3.7in/0.09398 m) and the freestream Mach number is 0.2. The CFD calculation employs the three-dimensional, time-dependent code CFL3D,[6,7] developed at NASA Langley Research Center to solve the three-dimensional, time-dependent, thin-layer Reynolds-Averaged Navier-Stokes (RANS) equations. A fine grid solution with 13.3 million
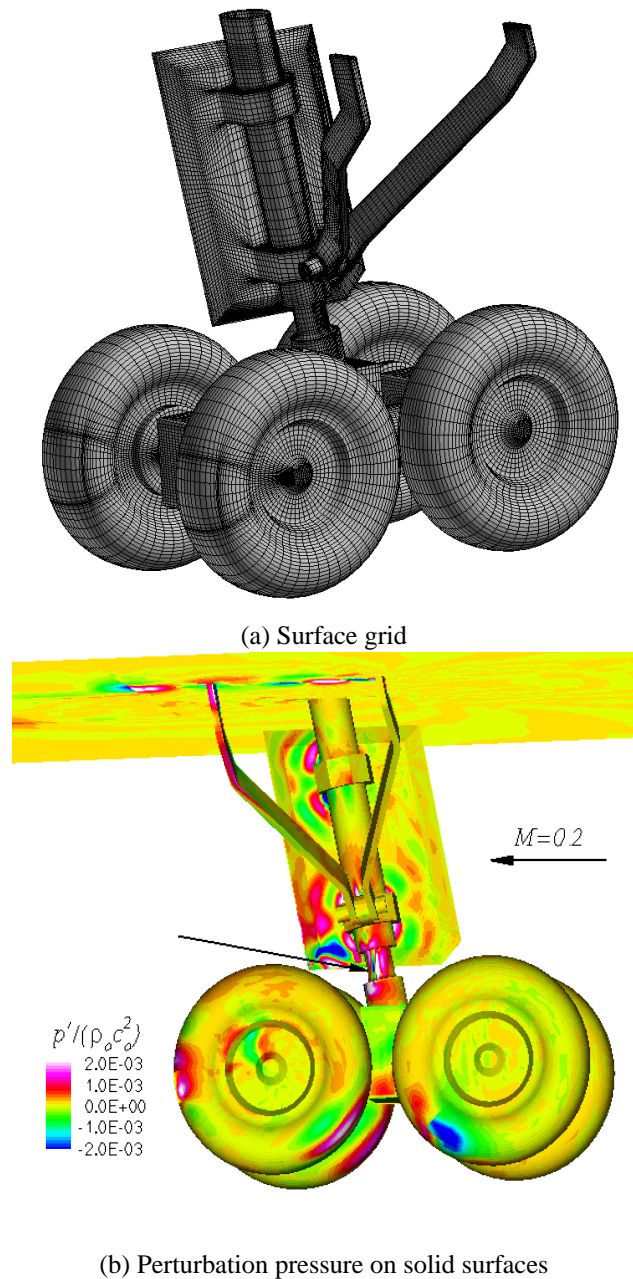

(a) Surface grid

(b) Perturbation pressure on solid surfaces

Fig. 1 CFD grid and results for a landing gear in a $M = 0.2$ flow.

grid points is ongoing due to the time-consuming nature of the simulation. To expedite our analysis, a medium grid has been constructed from the fine mesh by deleting every other grid point in each direction. The present preliminary analysis is based on the simulation obtained with this 1.8 million point, medium resolution grid. A more detailed discussion of the CFD calculation can be found in the paper by Li *et al.*[8]

Contours of the instantaneous perturbation pressure fluctuations on the gear solid surfaces are displayed in Figure 1(b). The surface pressure shows the footprint of the highly
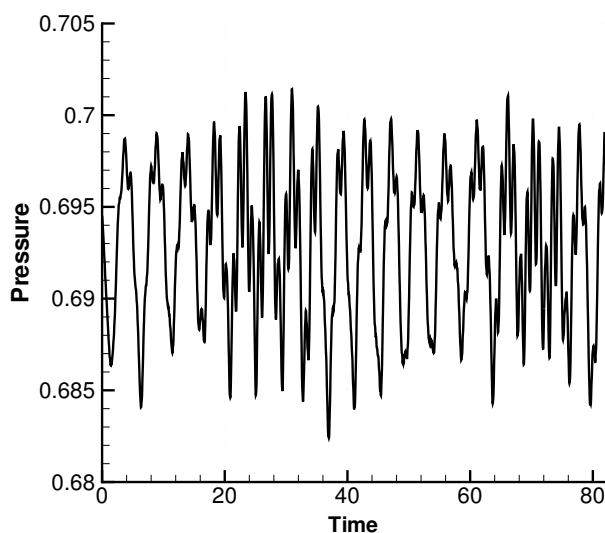
3

Fig. 2   Time history of the pressure on the oleo.

(a) Spectra

nonlinear and complicated interactive near-field flow dynamics. Lazos[9] investigated a similar four wheel landing gear experimentally and also found the flow around the wheels to be quite complicated. Figure 2 shows the time history of the pressure on the oleo in the contraction just below the door as indicated by the arrow in Figure 1(b). The pressure is nondimensionalized by $\rho_o c_o^2$. The time history shows the irregular character of the signal. The corresponding spectrum is shown as the broken line in Figure 3. The narrow band results have a bandwidth of 14.6 Hz. The large amplitude oscillations occur around 920 Hz and 3.8 kHz (model scale). The peak at 3.8 kHz actually varies between 3.5 and 4.5 kHz depending on what section of the oleo is used for the sample. Riding on top of these signals are two very high frequency oscillations generated by resonances in small, triangular shaped spaces between the yokes and the door. These spaces are found in the upper and lower yokes in both the upstream and downstream junctures with the door. The upstream and downstream cavities are slightly different in size, so the resonances occur at 20.2 kHz in the upstream cavities and at 24.7 kHz in the downstream ones. The wave pattern seen on the door in Figure 1(b) is caused by these tones.

Noise Calculations

The noise calculation involves 181 total subsurfaces comprising the data surface. All of the subsurfaces are impenetrable, so only the pressure histories are needed. 147 subsurfaces are on the gear itself and 34 are on the plate above the gear. The subsurfaces are a natural consequence of the block structured grid used for the CFD calculation. Each subsurface is a boundary of one of the 155 blocks comprising the grid. Because the problem is so large, the
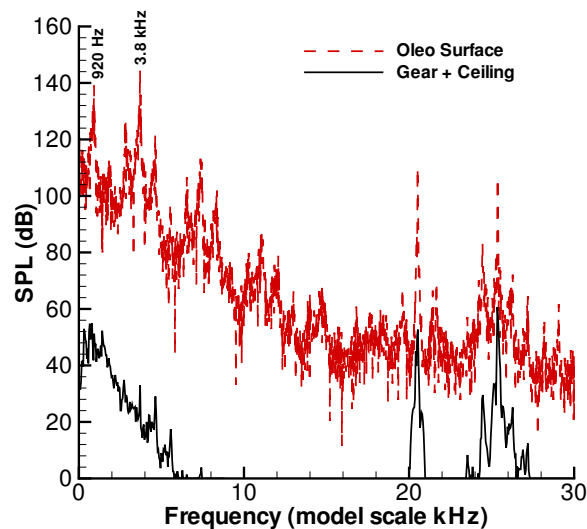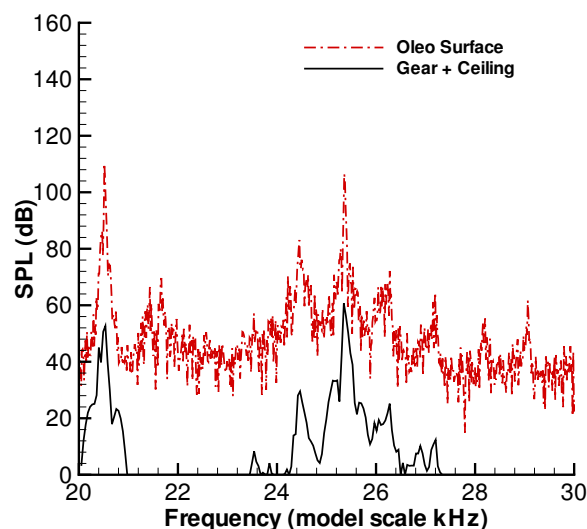
(b) High Frequencies

Fig. 3   Spectra of the pressure on the oleo compared with predictions for an observer 100 wheel diameters directly below the gear.

FW-H calculation would have to be performed on subsurfaces regardless of the grid topology. The complete time history record for all subsurfaces requires approximately 14 GB of disk space.

Over 12,000 nondimensional time samples with $l/c_o\Delta t = 0.02$ have been collected. The CFD simulation was sampled at every other time step. A Ffowcs Williams-Hawkings solver[2] written specifically for airframe noise applications is being used to perform the noise calculations. The calculated sound pressure level spectrum for an observer located directly underneath the gear is presented

4

in Figure 3 along with the sound pressure level on the oleo surface. The observer is located 100 wheel diameters away from the gear. All of the results in the paper represent an average over five time histories of 4096 samples each. Most of the noise is concentrated at low frequencies because of the absence of the smaller scale subcomponents in the model. However, two high-frequency tones are evident in the signal as shown if Figure 3(b). These tones are those caused by the resonances in the cavities between the yokes and the door. The correspondence between the 20.2 and 24.7 kHz peaks in the oleo surface and observer spectra are apparent even though the source of the noise is generated in the yoke-door juncture. This signal is quite strong and can be observed in the pressure signal over most of the gear.

Subsurface Noise Predictions

Although much of the smaller scale detail is missing from this gear model, the frequency content below 6 kHz is relatively rich and it is not apparent which components are contributing to the different portions of the spectrum. There are several distinct tones that are probably the result of shedding from different components. To investigate the source of the different peaks, the landing gear was divided into 10 regions as show in figure 4. Each region is colored differently to identify each of the subdomains.
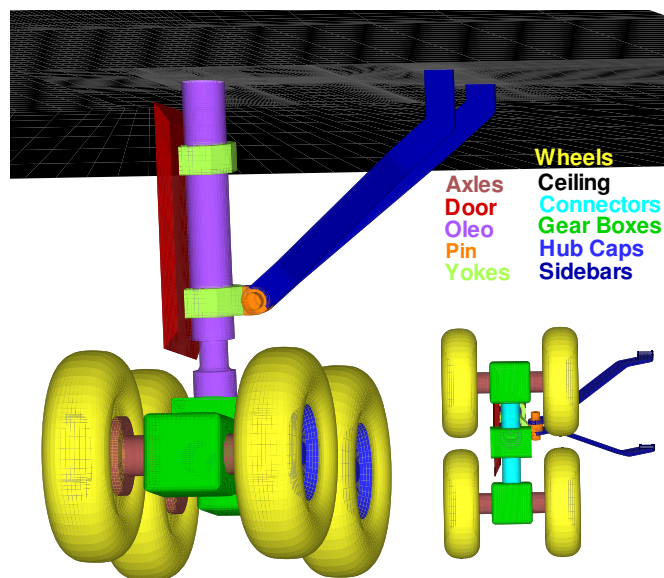

Fig. 4   Landing gear colored by component.

The prediction using all of the surfaces (Gear + Ceiling) is compared with the results when using the ceiling, and everything except the ceiling (No Ceiling) in Figure 5. The results are for an observer located 100 wheel diameters directly below the gear. The results do vary with observer position, but the general trends are similar at most observer locations of interest. The figure shows that below 4 kHz, the ceiling accounts for almost all of the noise. The signal

from the gear components is nearly 10 dB lower than that of the ceiling. Although one would expect the ceiling to be important because of reflections, it should not be dominant. A calculation without the ceiling where all of the gear components are mirrored still does not produce levels anywhere near those observed with the ceiling alone. Clearly, the ceiling is acting as more than just a reflector as is borne out by Figure 6 that shows the instantaneous perturbation pressure contours on the gear and ceiling looking from below. The most intense fluctuations occur on the ceiling in the wake of the sidebars. Although it is likely that the wake from the sidebars would interact with the ceiling, the fluctuations are actually being amplified across and along block boundaries because of insufficient grid resolution. Each of the discontinuities in the contours in Figure 6 represents a block interface where extensive patching is used to reduce the number of grid points. Because it cannot be determined how much unrealistic amplification is occurring, the prediction when the ceiling is excluded will be used as a reference in the remainder of the paper.
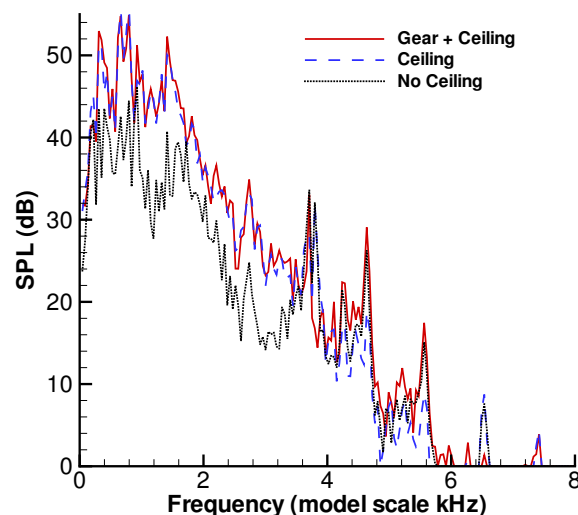

Fig. 5   FW-H results for an observer 100 wheel diameters directly below the landing gear in a $M = 0.2$ flow.

The predicted noise for each of the subsurfaces in Figure 4 is shown in Figures 7(a)-(c). The spectra are divided between the three plots for clarity. The reference calculation without the ceiling is shown on all three plots. Figure 7(a) suggests that the gear boxes and the connectors between them are primarily responsible for the broadband component of the noise. The connectors radiate most strongly between 1 and 4 kHz; whereas, the gear boxes are important at all frequencies up to 6 kHz. The gear boxes are also responsible for tones at 170 Hz, 310 Hz, 930 Hz, 3.7 kHz, and 5.6 kHz. The pin connecting the sidebars to the yoke also contributes at 930 Hz, but is almost negligible at all
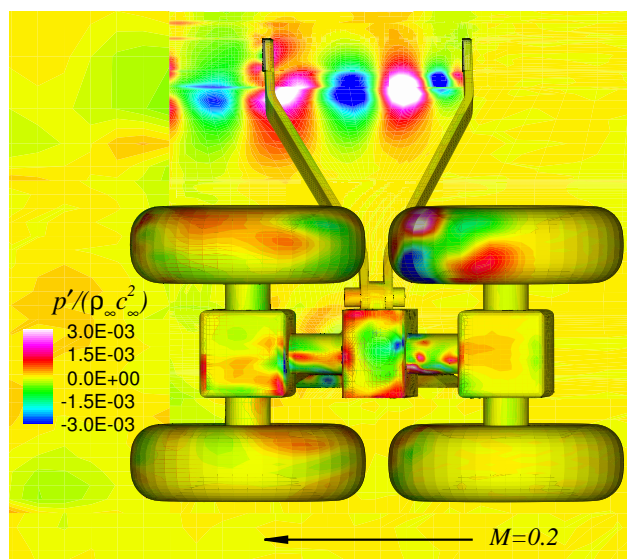
**Fig. 6 Instantaneous pressure contours on a landing gear in a $M = 0.2$ flow.**

other frequencies. Figure 7(b) shows that the levels associated with the wheels, axles, and hub cups are somewhat lower than that of the gear boxes, and the signals appear to be even more tonal. The hub caps do not appear to be important for this simplified gear. The wheels appear to be the strongest radiator of the group, with tones at 430 Hz and 930 Hz. The axles make a significant contribution to the lower frequencies, and are partially responsible for a tone at 3.7 kHz. The spectra of the subsurfaces investigated in Figure 7(c) are almost completely comprised of tones. The oleo is the dominant member of the group with strong tones at 930 Hz and 3.7 kHz. Higher harmonics of the 930 Hz tone can be observed out to 5.5 kHz. The spectra for the door and yoke also show a spike around 930 Hz, but this is likely because of their proximity to the oleo. The yokes also make a strong contribution to the 3.8 kHz tone. The sidebars are responsible for the tones at 670 Hz and 795 Hz, but there is clearly a great disparity with the ceiling spectrum in Figure 5. One would expect a stronger correspondence if the interaction of shed vortices from the sidebars with the ceiling were responsible for the broadly elevated levels associated with the ceiling.

FW-H Integrand Strengths

The subsurface spectra have given an indication of what components are responsible for the different features in the overall spectrum. The source localization can be further refined by plotting the integrand function of Equation 5 over the gear for different frequencies of interest. Figure 8 shows the results for frequencies of 353 Hz and 795 Hz. The primary view is at a slight angle from under the gear, and the superimposed image is a view from the side. The amplitudes are dimensionless, and should only be used to make relative comparisons. At 353 Hz, the overall spec-
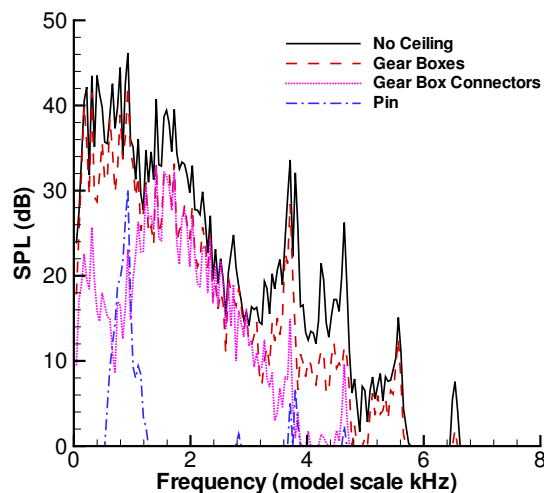

(a)
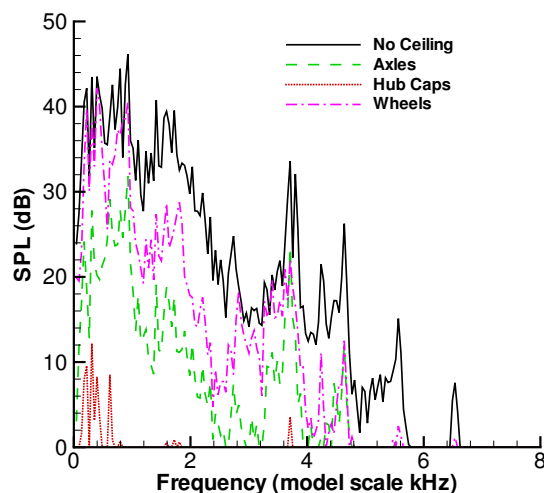
(b)
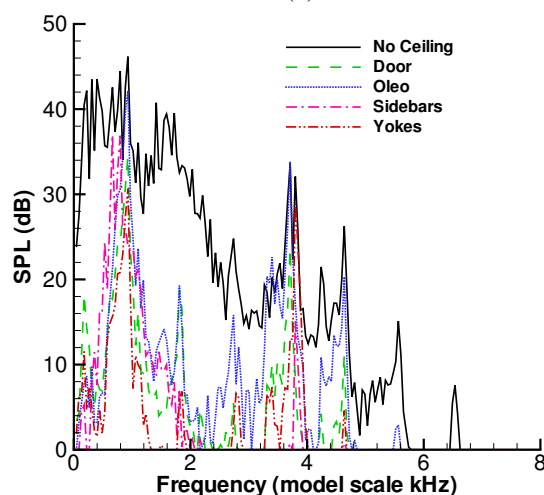
(c)

Fig. 7 FW-H results for an observer 100 wheel diameters directly below the landing gear in a $M = 0.2$ flow.

trum with the ceiling has a tone; whereas, the spectrum when the ceiling is excluded is at a local minimum. Figure 8(a) shows that almost all of the regions responsible for the 353 Hz signal are on the ceiling. Unfortunately, these regions are located at block interface boundaries which are shown as black lines in the figure. Alternating grid lines in the mesh are shown in gray. The long streak that starts midway between the two sidebars originates near a tee in the boundaries, below which the grid is relatively coarse. The two intense regions downstream of the sidebars also occur at patched boundaries where the grid coarsens significantly.

The overall spectrum reaches a maximum value at 795 Hz, and the spectrum for the sidebars shows a tone at this frequency. However, Figure 8(b) shows that the ceiling is primarily responsible for the peak. The intense region between the sidebars is centered around a block interface. In addition, the peak region downstream of the sidebars occurs where the grid coarsens. The high values on the underside of the downstream sidebar indicate that there is some shedding from the sidebars at this frequency, but it appears to be artificially amplified at the block boundaries. There is also some indication that the upper portion of the rear wheels are important sources at this frequency.

Figure 9 shows the results for 927 Hz and 1413 Hz. The most intense regions now occur on other components than the ceiling, but the ceiling is still dominant because the area over which it has significant levels of the integrand is large. At 927 Hz, the transition region around the contraction in the oleo is the most intense region. There is also a significant contribution from the door, but this is most likely just a reflection of the oleo source. Furthermore, the intense region on the door ends abruptly at block interfaces indicating some effect of the grid. The intense regions on the wheels may also be caused by reflections of the oleo source. At 1413 Hz, the underside of the middle gear box and the connector between the upstream two gear boxes show the highest levels. This region is important over a wide range of frequencies as can be seen in Figures 8 and 9.

At higher frequencies, the influence of the ceiling diminishes, and the other sources become more apparent. At 3798 Hz, Figure 10(a) shows that there are intense fluctuations around the oleo contraction. This signal is not present on the opposite side of the oleo indicating that this is not simple vortex shedding. The vertical line of intense source on the oleo actually extends above the lower yoke; however, the strongest fluctuations are on the oleo contraction. Although it is difficult to see from the figure, the entire underside of the lower yoke has very high levels. The spectrum for the yoke subsurfaces shown in Figure 7(b) showed a strong peak at 3798 Hz, but it may be simply acting as a reflector for what is occurring near the oleo. At 4637 Hz, the oleo contraction is again an important source region, as well as the connector between the upstream two gear boxes. The ceiling appears to have a reasonable noise footprint at
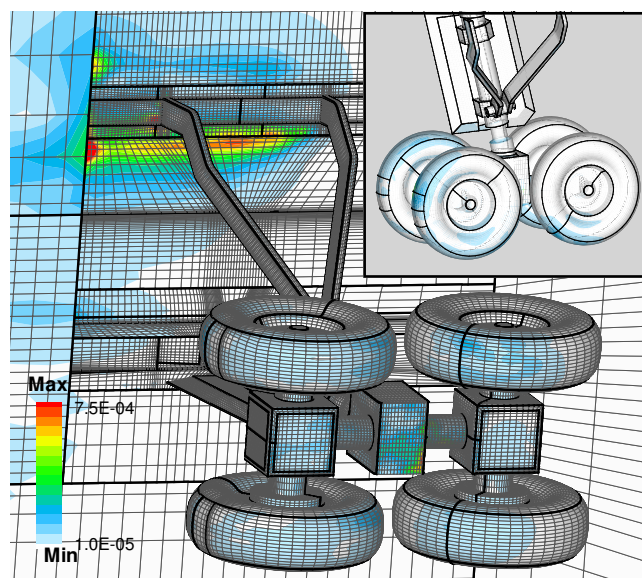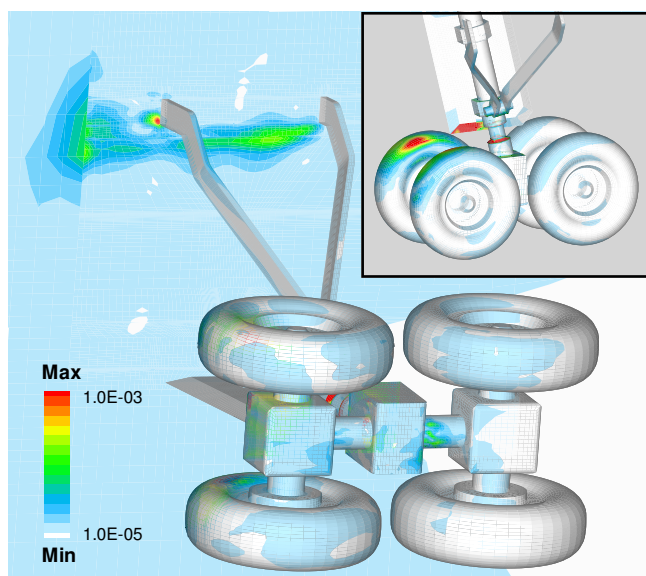

(a) 353 Hz
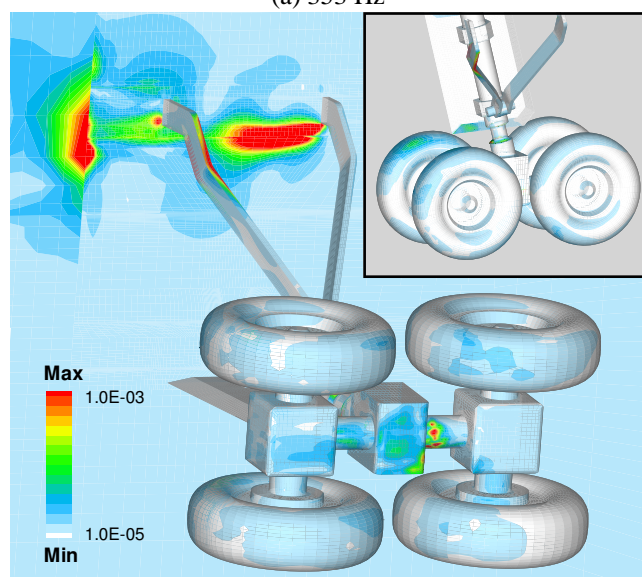
(b) 795 Hz

Fig. 8 FW-H source strengths plotted over the surface of the landing gear. The observer is 100 wheel diameters directly below the gear in a $M = 0.2$ flow.

this frequency, but this may be the result of the grid being too coarse resulting in excessive dissipation for short wavelengths.
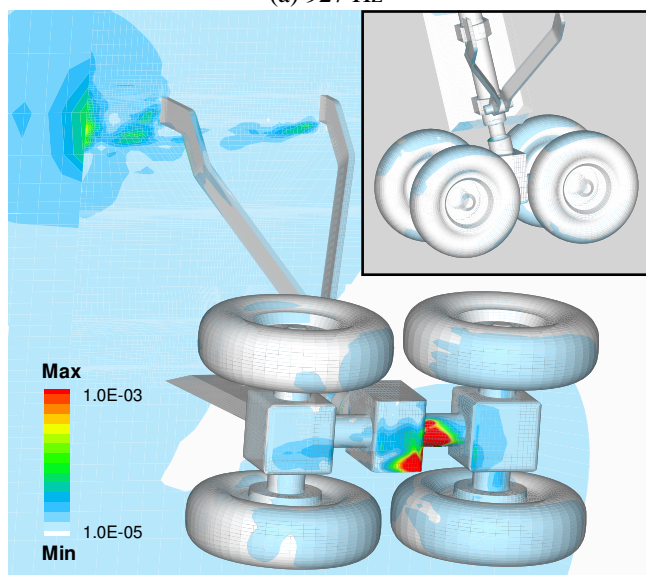
Directivity

As a final demonstration of the capabilities of the FW-H prediction method, the directivity was calculated using 345 observer locations spaced uniformly on a hemisphere with a radius of 100 wheel diameters. Figure 11 shows the results with and without the ceiling. The plots represent the energy from all frequencies below 8 kHz. The hemisphere is being viewed from above with the flow from left to right.
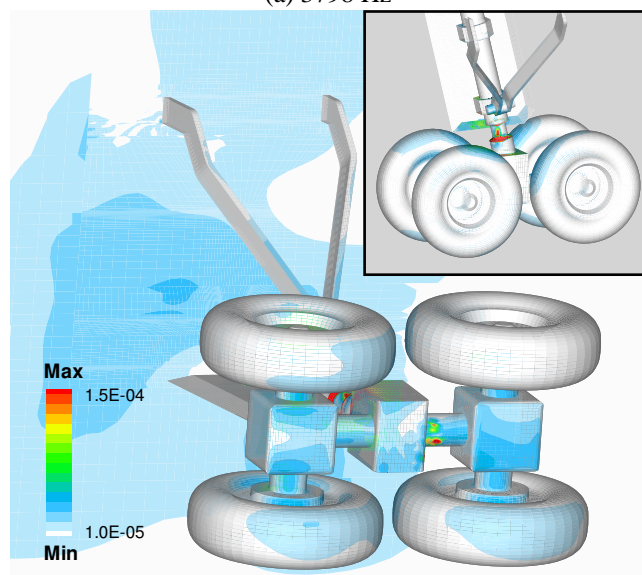
(a) 927 Hz
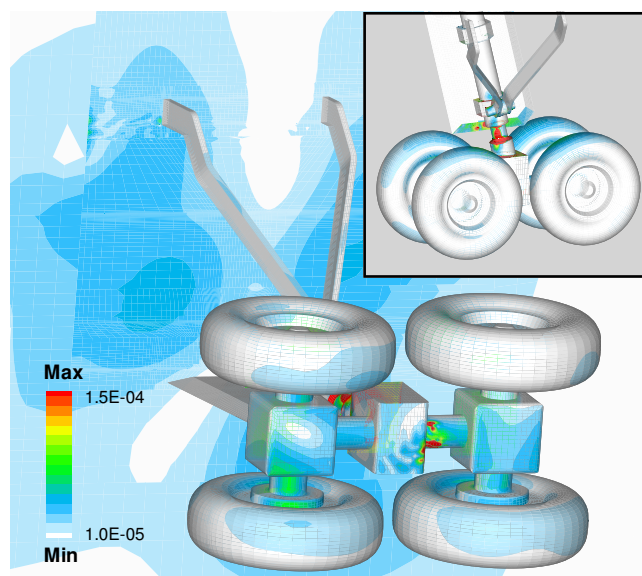
(b) 1413 Hz

Fig. 9   FW-H source strengths plotted over the surface of the landing gear. The observer is 100 wheel diameters directly below the gear in a $M = 0.2$ flow.

(a) 3798 Hz

(b) 4637 Hz

Fig. 10   FW-H source strengths plotted over the surface of the landing gear. The observer is 100 wheel diameters directly below the gear in a $M = 0.2$ flow.
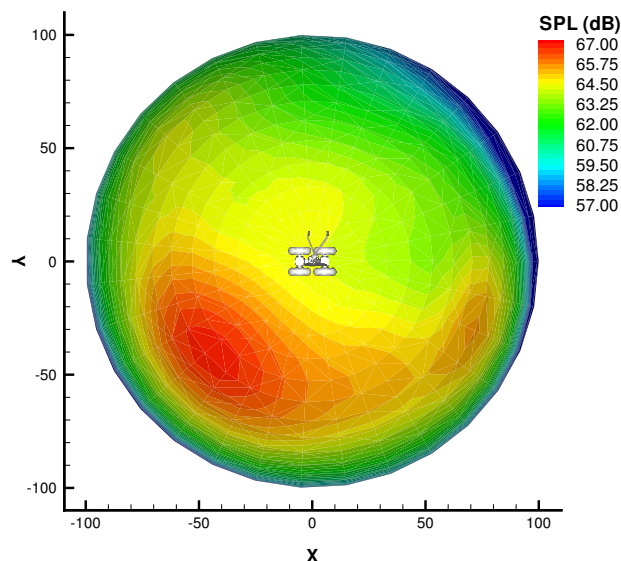
The gear is superimposed to orient the reader. The directivity when the ceiling is included shows a peak upstream of the gear to the door side. The directivity without the ceiling shows more radiation normal to the oleo with the primary radiation occurring opposite the door. Most likely, the directivity with the ceiling included is just an artifact of the phasing of the artificial sources on the ceiling. Figure 12 shows the real component of the FW-H integrand plotted over the gear. In Figures 8 to 10, the amplitude of the complex integrand was plotted, but the phase is important when the contributions are summed. As Figure 12 clearly shows, there is considerable difference in the phase of the signal
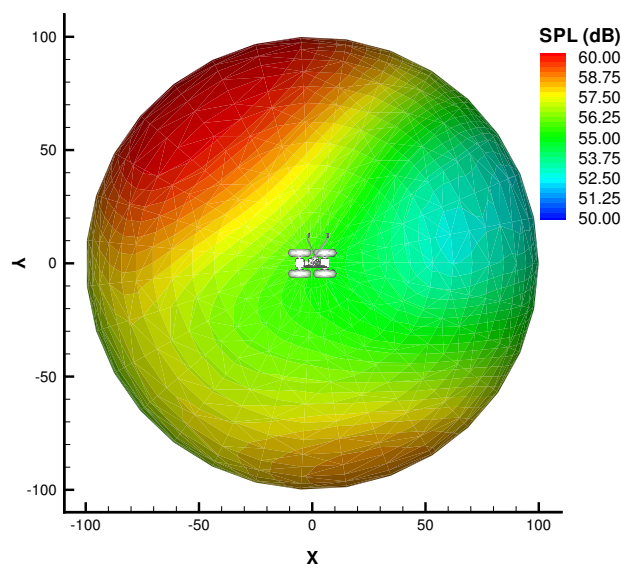
on the ceiling, and the peak in the directivity is just the location where the summation happens to be a maximum. The directivity without the ceiling is missing the important effect of reflection by the ceiling, so the true directivity has yet to be determined.

Source Identification

Actual source identification requires investigating the flow itself rather than on just looking at the pressure footprint on solid surfaces. Bluff body separation and the formation of vortical structures are often responsible for strong fluctuations. Vortex shedding off of various com-

(a) Gear + Ceiling

(b) Gear

Fig. 11   Comparison of predicted directivity for observers on a hemisphere 100 wheel diameters from the mounting point of the gear oleo. The three-dimensional representation is being viewed from above the gear with the flow from left to right.
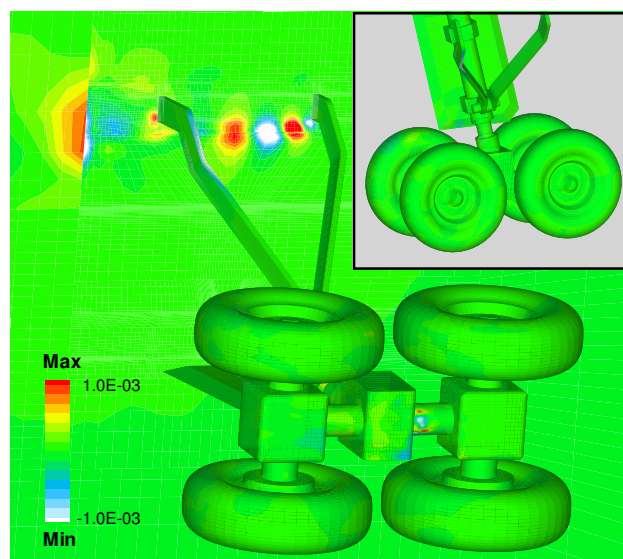

Fig. 12   The real components of the FW-H source strength plotted over the surface of the landing gear. The observer is 100 wheel diameters directly below the gear in a $M = 0.2$ flow. The frequency is 795 Hz.

ding. Part of the wake behind the upstream sidebar also appears steady. The portion farthest from the door has negative signed vorticity (colored black and blue) and appears very smooth. No sources were identified in that region in Figures 8 to 10. A recirculation bubble does exist behind the sidebar in the region colored black, but very little vorticity is shed downstream. However, the white and red colored portion of the wake does show signs of nonuniformities that are indicative of discrete vortices and unsteadiness. Animations of the vorticity have revealed that the waviness in the plot is because of traveling vortices, but the large discontinuities are caused by numerical errors at the grid block interfaces. There does appear to be a real noise source in this region, but it is artificially amplified to a level that may be overwhelming all of the real sources. The abrupt disappearance of all vorticity downstream of the sidebars is another indication that the source in this interface region is fictitious. The discontinuities in figure 13 are accentuated because they involve derivatives of the primitive variables, but the errors are clearly large enough to produce erroneous pressure signals on the ceiling. Although patched interfaces exist throughout the grid, it is unclear what effect they are having on other gear components. The grid is much finer over the gear itself, so any errors are expected to be less severe.

Figure 14 presents the vertical component of vorticity in a plane just below the connectors between the gear boxes. The vorticity field between the middle and upstream gear boxes is very irregular; whereas, the flow behind the middle gear box shows a recirculating pattern that appears steady. This agrees with the results in Figure 9(b) which identified the region around the front connector as a strong noise

ponents is expected to be a primary source of noise for a landing gear. Figure 13 presents an instantaneous view of the the vertical component of vorticity in a plane just below the ceiling. It cannot be determined from the plot whether the vorticity is steady, but there will typically be some indication of discrete vortices in an unsteady wake. Hence, the wake behind the oleo appears to be steady. The door is attached to one side of the oleo preventing typical shed-
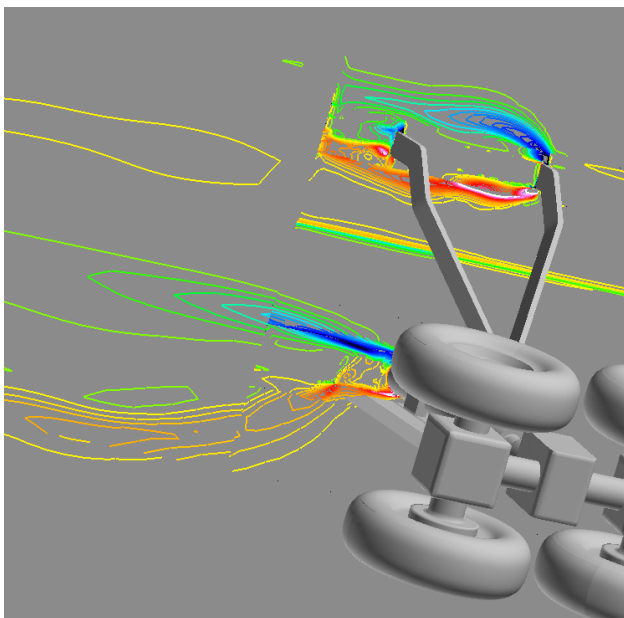
9

Fig. 13 Instantaneous view of the vertical component of vorticity in a plane just below the ceiling.

source. The vorticity around the tires in this plane is relatively steady. Most of the shedding around the tires occurs closer to the tops and bottoms.
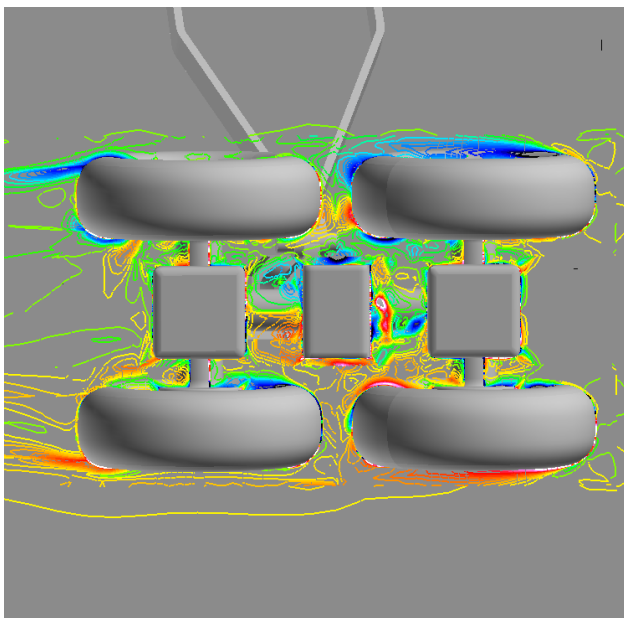

Fig. 14 Instantaneous view of the vertical component of vorticity in a plane just below the connectors between the gear boxes. The flow is from right to left.

The oleo was also identified as a region with intense source strength, and Figure 15 confirms that there is vortex shedding in the vicinity of the oleo contraction. The horizontal plane is just below the upper contraction in the oleo. The alternating signed vorticity in the wake is indicative of vortex shedding, and it is clear that some interaction

is occurring with the door. The flow is actually even more complicated than the figure reveals as the character of the shedding is very different in the center of the contraction from that where the contraction occurs.

Figure 15 also shows the vorticity in a plane perpendicular to the door that passes in between the two sidebars. In the region above the yoke, the flow is quite complicated, but it is not as efficient of a noise source as the oleo itself.

Although the vorticity plots do seem to confirm that there are significant vortical fluctuations in the regions where the analysis indicates the noise is being generated, further study is required to understand all of the phenomena involved.
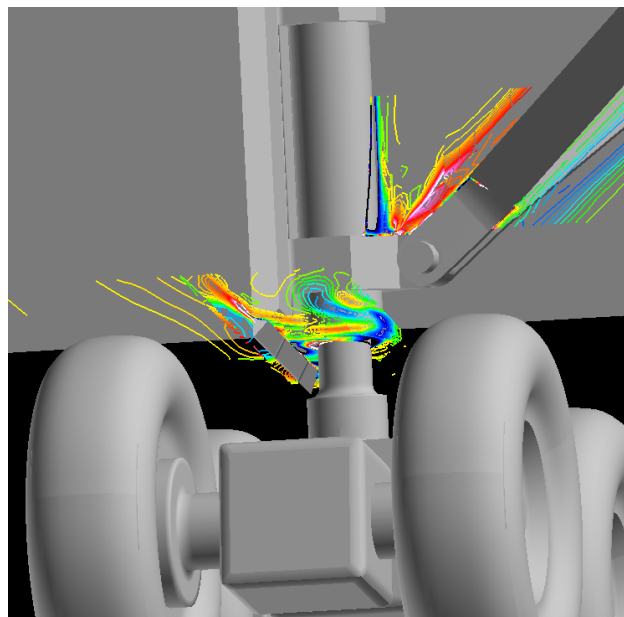

Fig. 15 Instantaneous view of the vertical component of vorticity in planes just below the contraction in the oleo and perpendicular to the door between the two sidebars.

Conclusions

The investigation presented in this paper represents the first step toward landing gear noise prediction using large scale computation and the acoustic analogy. Even though significant resources were used during the current calculations, some important features were not captured. Most of the high frequency part of the spectrum was missed because of the simplified nature of the landing gear. If we consider the model to be 10% of full scale, then the calculation has only captured full scale frequencies below 600 Hz. Clearly, it is desirable to extend the range of resolved frequencies which would require more grid points and a much more complicated mesh. The structured grid required 155 blocks for the current model, so it would be difficult for a structured grid technique to be used for a more realistic model. Furthermore, unsteady numerical errors were identified in the vicinity of patched block interfaces. These interfaces

would be sufficient for a steady problem and were often away from any solid surfaces, so extra care must be taken to insure sufficient resolution almost throughout the entire flowfield when doing an unsteady noise calculation. The mesh used in the current investigation has half the resolution of a grid being employed in another computation. Although similar numerical errors are present on the finer mesh, their influence on the solution appears to be much smaller.

Despite the difficulties, the current analysis has added some insight into the flow dynamics generating the low frequency noise. Employing a Ffowcs Williams and Hawkings solver using subsurfaces and plotting the integrand is useful for identifying potential noise sources. Combining the noise source information with extracted flow features in the vicinity of these potential sources can reveal what is causing the noise. For the simplified gear, the flow around the gear boxes and the connectors between them appears to be responsible for the underlying shape of the spectrum. Most of the unsteadiness is in a separated region between the middle and upstream gear boxes where strong, irregular vorticity is produced. Many of the gear components produce tones, but the oleo generates two loud tones along with their harmonics. The flow over the part of the oleo attached to the door appears to be relatively steady and not an effective noise radiator. However, below the door, cylinder shedding does occur. Some of the noise is caused by vortex shedding, but the flow is considerably more complicated because of the proximity of the door as well as the effect of the contraction in the oleo. A more detailed analysis of the unsteady flow field is required to better understand the fluid dynamics responsible for noise generation in this region. Typically, only instantaneous snapshots of the volume flow are available for such studies which makes it difficult to identify all of the relevant phenomena.

References

[1]Ffowcs Williams, J. E. and Hawkings, D. L., "Sound generation by turbulence and surfaces in arbitrary motion," *Philosophical Transactions of the Royal Society of London A*, Vol. 342, 1969, pp. 264–321.

[2]Lockard, D., "A Comparison of Ffowcs Williams-Hawkings Solvers for Airframe Noise Applications," AIAA Paper 2002-2580, Eighth AIAA/CEAS Aeroacoustics Conference, Breckenridge, CO, June 17–19, 2002.

[3]Crighton, D. G., Dowling, A. P., Ffowcs Williams, J. E., Heckl, M., and Leppington, F. G., *Modern Methods in Analytical Acoustics*, chap. 11, Springer-Verlag, London, 1992, pp. 334–342.

[4]Farassat, F., "Linear Acoustic Formulas for Calculation of Rotating Blade Noise," *AIAA Journal*, Vol. 19, No. 9, 1981, pp. 1122–1120.

[5]Souliez, F. J., Long, L. N., Morris, P. J., and Sharma, A., "Landing Gear Aerodynamic Noise Prediction Using Unstructured Grids," *International Journal of Aeroacoustics*, Vol. 1, No. 2, 2002, pp. 115–135.

[6]Rumsey, C., Biedron, R., and Thomas, J., "CFL3D: Its History and Some Recent Applications," TM 112861, NASA, May 1997, presented at the Godonov's Method for Gas Dynamics Symposium, Ann Arbor, MI.

[7]Krist, S. L., Biedron, R. T., and Rumsey, C., "NASA Langley Research Center: Aerodynamic and Acoustic Methods Branch," *CFL3D User's Manual (Version 5)*, 1997.

[8]Li, F., Khorrami, M. R., and Malik, M. R., "Unsteady Simulations of a Landing-Gear Flow Field," AIAA Paper 2002-2411, Eighth AIAA/CEAS Aeroacoustics Conference, Breckenridge, CO, June 17–19, 2002.

[9]Lazos, B., "Surface Topology on the Wheels of a Generic Four-Wheel Landing Gear," *AIAA Journal*, Vol. 40, No. 14, 2002, pp. 2402–2411.